Acta Pharmaceutica Sinica B 2022;12(9):3710–3725

Chinese Pharmaceutical Association
Institute of Materia Medica, Chinese Academy of Medical Sciences

Acta Pharmaceutica Sinica B

www.elsevier.com/locate/apsb
www.sciencedirect.com

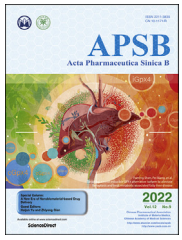

ORIGINAL ARTICLE

Cooperative coordination-mediated multi-component self-assembly of "all-in-one" nanospike theranostic nano-platform for MRI-guided synergistic therapy against breast cancer

Xiaojie Chen[a,b,†], Xudong Fan[a,†], Yue Zhang[a], Yinghui Wei[a], Hangsheng Zheng[a], Dandan Bao[d], Hengwu Xu[f], Ji-Gang Piao[a,b,e,*], Fanzhu Li[a,b,*], Hongyue Zheng[c,*]

[a]*School of Pharmaceutical Sciences, Zhejiang Chinese Medical University, Hangzhou 310053, China*
[b]*Key Laboratory of Neuropharmacology and Translational Medicine of Zhejiang Province, School of Pharmaceutical Sciences, Zhejiang Chinese Medical University, Hangzhou 310053, China*
[c]*Libraries of Zhejiang Chinese Medical University, Zhejiang Chinese Medical University, Hangzhou 310053, China*
[d]*Department of Dermatology & Cosmetology, The First Affiliated Hospital of Zhejiang Chinese Medical University (Zhejiang Provincial Hospital of Traditional Chinese Medicine), Hangzhou 310006, China*
[e]*Academy of Chinese Medical Sciences, Zhejiang Chinese Medical University, Hangzhou 310053, China*
[f]*Department of Pharmacy, Jinhua People's Hospital, Jinhua 321000, China*

Received 30 September 2021; received in revised form 19 December 2021; accepted 21 February 2022

KEY WORDS

Carrier-free nanodrugs;
Self-assembly;
Nanospike;
Magnetic resonance imaging;
Tumor microenvironment-responsive;
Deep penetration;

Abstract Carrier-free multi-component self-assembled nano-systems have attracted widespread attention owing to their easy preparation, high drug-loading efficiency, and excellent therapeutic efficacy. Herein, MnAs-ICG nanospike was generated by self-assembly of indocyanine green (ICG), manganese ions (Mn^{2+}), and arsenate (AsO_4^{3-}) based on electrostatic and coordination interactions, effectively integrating the bimodal imaging ability of magnetic resonance imaging (MRI) and fluorescence (FL) imaging-guided synergistic therapy of photothermal/chemo/chemodynamic therapy within an "all-in-one" theranostic nano-platform. The as-prepared MnAs-ICG nanospike had a uniform size, well-defined nanospike morphology, and impressive loading capacities. The MnAs-ICG nanospike exhibited sensitive responsiveness to the acidic tumor microenvironment with morphological transformation and

*Corresponding authors.
E-mail addresses: jgpiao@zcmu.edu.cn (Ji-Gang Piao), lifanzhu@zcmu.edu.cn (Fanzhu Li), zhy@zcmu.edu.cn (Hongyue Zheng).
[†]These authors made equal contributions to this work.

Peer review under responsibility of Chinese Pharmaceutical Association and Institute of Materia Medica, Chinese Academy of Medical Sciences.

https://doi.org/10.1016/j.apsb.2022.02.027

2211-3835 © 2022 Chinese Pharmaceutical Association and Institute of Materia Medica, Chinese Academy of Medical Sciences. Production and hosting by Elsevier B.V. This is an open access article under the CC BY-NC-ND license (http://creativecommons.org/licenses/by-nc-nd/4.0/).

Synergistic therapy;
Breast cancer

dimensional variability, enabling deep penetration into tumor tissue and on-demand release of functional therapeutic components. *In vitro* and *in vivo* results revealed that MnAs-ICG nanospike showed synergistic tumor-killing effect, prolonged blood circulation and increased tumor accumulation compared to their individual components, effectively resulting in synergistic therapy of photothermal/chemo/chemodynamic therapy with excellent anti-tumor effect. Taken together, this new strategy might hold great promise for rationally engineering multifunctional theranostic nano-platforms for breast cancer treatment.

© 2022 Chinese Pharmaceutical Association and Institute of Materia Medica, Chinese Academy of Medical Sciences. Production and hosting by Elsevier B.V. This is an open access article under the CC BY-NC-ND license (http://creativecommons.org/licenses/by-nc-nd/4.0/).

1. Introduction

Cancer is the leading cause of disease-related death around the world, among which breast cancer has become the most common malignancy since 2020[1]. The efficient integration of multiple anti-tumor therapeutic modalities and medical diagnostics within multifunctional theranostic nano-platforms with tailored pharmaceutical behavior, enhanced therapeutic efficacy, improved tumor specificity, and reduced adverse side effects has proven a promising strategy for cancer therapy. Zhang et al.[2] has reported a multicomponent nano-platform based on the amphiphilic amino-acid coordinated self-assembly of metal ions with the simultaneous encapsulation of photosensitive drugs to generate Fmoc-$_L$-L/Mn^{2+}/Ce6 nanoparticles (FMCNPs) capable of magnetic resonance imaging (MRI)-guided photodynamic therapy (PDT) for cancer therapy. Dong et al.[3] constructed a safe multifunctional nano-platform based on polydopamine nanoparticles as a versatile carrier loading with indocyanine green (ICG), doxorubicin (DOX), and manganese ions for MRI-guided chemo & photothermal cancer therapy. However, it remains some challenges in the development of multifunctional anti-tumor nano-platforms. Between them, the paradox between particle size and tumor penetration and blood circulation has dramatically hindered the treatment efficacy, requiring intelligent size-variable nano-systems for enhanced tumor accumulation and deep tumor penetration.

Recently, carrier-free nanodrugs have drawn considerable attention. Compared to carrier-assistant drug delivery systems, carrier-free nanodrugs have excellent flexibility and changeability, low systemic toxicity, high drug loading capability, stimulus sensitive features, and synergistic therapeutic efficacy[4], facilitating their applications in cancer treatment. Qin et al.[5] have reported a self-delivery supramolecular nano-platform which constructed *via* the host−guest interaction between chlorine 6-conjugated β-cyclodextrin and ferrocene-modified conjugates to form an inclusion complex to fulfill self-amplified PDT for anti-tumor therapy. Lin et al.[6] incorporated chemotherapeutic agent paclitaxel (PTX) and photosensitizer ICG into one carrier-free nanodrug (PTX/ICG NDs) *via* self-assembly to realize chemo-photothermal synergistic therapy. Hence, the development and application of multifunctional carrier-free nanodrugs is an important research direction in the field of nanobiology[7].

With the enormous progress in nanomedicine-mediated cancer therapy, various therapeutic methods have been exploited in breast cancer treatment. As a non-invasive and spatio-temporally controlled therapeutic strategy, photothermal therapy (PTT) has been extensively used in breast cancer treatment *via* light-converting agent-mediated localized photothermal tumor ablation under the stimulation of near-infrared (NIR) laser[8−12]. PTT has demonstrated a significant combinational effect with chemotherapy, chemodynamic therapy (CDT), or immunotherapy, representing an adaptable avenue to overcome the limitation of monotherapy[3,13−16]. ICG is an NIR fluorescent dye for both fluorescence (FL) imaging and PTT approved by U.S. Food and Drug Administration (FDA), while suffering from rapid *in vivo* elimination and unavoidable photobleaching[17]. Hence, how to effectively apply ICG in breast cancer treatment remains challenging.

Arsenic trioxide (ATO) is an FDA-approved chemotherapeutic agent in the first-line treatment of acute promyelocytic leukemia (APL) with clarified pharmacology[18]. The use of ATO has also been extended to multiple solid tumors, including breast, liver, lung, and glioma[19−23]. However, the clinical application of ATO has been impeded by its rapid renal clearance and severe systemic toxicity. In recent years, several types of nano-vehicles such as liposomes, polymer micelles, and mesoporous silica were fabricated to deliver ATO into the tumor site, while are limited by low drug-loading efficiency, complex preparation process, and undesirable leakage of ATO during circulation[22,24−26]. Pentavalent arsenate [As (V)] is an important biological oxidation state of arsenic with less systemic toxicity as well as weakened therapeutic efficacy[27,28]. As a bioactivitable “prodrug” of trivalent arsenite [As (III)], As (V) can be transformed to the more toxic ATO under the stimulation of hypoxia, high glutathione (GSH) level, or mild acidity of tumor microenvironment (TME)[28,29]. Based on the fact that single treatment with As (III) or As (V) failed to provide sufficient beneficial effects for treatment for solid tumor, effective partners were therefore needed to cooperate against solid tumors[30].

Given the characteristic features of the mild acidity and hydrogen peroxide (H_2O_2) overproduction of the TME and the high toxicity of hydroxyl radicals (·OH)[31−33], CDT has been demonstrated as an emerging therapeutic modality and a promising strategy to trigger apoptosis of cancer cells that can convert H_2O_2 to ·OH *via* valence-variable metal ion-mediated Fenton or Fenton-like reaction[34]. Among the most frequently utilized metal ions for CDT (Fe, Cu, Mn, Co, and Ce), manganese ion (Mn^{2+}) is highly favored for its intrinsic biocompatibility, high reactivity towards Fenton-like reaction, and excellent contrast ability for MRI[35−38], which has become one of the most commonly adopted medical imaging technologies in clinical treatment[39]. Mn^{2+} was

reported to co-precipitate with arsenite (AsO_3^{3-}) to form manganese arsenite complex (MnAs) *via* electrostatic interaction, stable at neutral pH and dissociates in an acidic environment, with elevated drug-loading efficiency and controlled release of ATO[40–42]. Mn^{2+} can also self-assemble with ICG through coordination interactions to form a 1D nanofiber-like structure with enhanced therapeutic efficacy[43]. These results imply that Mn^{2+} could act as a prospective bridging ligand *via* concomitant interaction with ICG and ATO to efficiently integrate multifunctional components within a theranostic nano-platform.

It has been reported that, reactive oxygen species (ROS) and GSH, which is the most overabundant antioxidant cofactor within TME, play critical roles in cancer-related redox homeostasis regulation[44,45], and maintain the redox balance of TME[38]. In addition, GSH is a scavenger to counteract intracellular ROS and confers resistant capacity of chemo-, radio-, and photodynamic therapy[35]. In addition, the elevated ROS and GSH concentrations in the TME also contributed to the drug resistance of tumors[46]. Hence, breaking the dynamic equilibrium of redox *via* GSH depletion and elevating intracellular ROS level in the meantime would be a potential strategy for anti-tumor treatment[47].

Herein, an "all-in-one" theranostic nano-platform (MnAs-ICG nanospike) was constructed in this study. Employing electrostatic and coordination interactions, Mn^{2+}, arsenate (AsO_4^{3-}), and ICG could be efficiently chelated and competitively coordinated, acting as a multifunctional nano-platform towards MRI-guided photothermal/chemo/chemodynamic synergistic therapy. Firstly, the MnAs-ICG nanospike sensitively responded to the acidic TME, collapsing and then dissociating into nanoparticles with a much smaller diameter, which could efficiently penetrate deep into the tumor tissue, accompanied by the on-demand release of Mn^{2+}, AsO_4^{3-}, and ICG. In addition, under the guidance of T_1-weighted MRI for real-time monitoring, Mn^{2+} could convert H_2O_2 into highly toxic ·OH through Fenton-like reaction. Through the combination of PTT, higher temperature could accelerate ·OH formation and promote AsO_4^{3-} endocytosis, leading to improved CDT and chemotherapy efficiency[48]. Finally, AsO_4^{3-} would be converted to more toxic AsO_3^{3-} with the assistance of GSH in TME, which is 5–10-fold higher than normal cells[47]. Accordingly, this "all in one" theranostic nano-platform works *via* cascade reactions based on the feature of TME, including Mn^{2+}-mediated CDT, ICG-mediated PTT, and AsO_4^{3-}-mediated chemotherapy, presenting excellent synergistic therapy. The therapeutic combination developed here represents a novel strategy for breast cancer treatment.

2. Materials and methods

2.1. Materials

Manganese chloride tetrahydrate ($MnCl_2 \cdot 4H_2O$) was purchased from Macklin (Shanghai, China). $HAsNa_2O_4 \cdot 7H_2O$, 5,5-dimethyl-pyrroline-*N*-oxide (DMPO), amiloride hydrochloride and chlorpromazine hydrochloride were bought from Sigma-Aldrich (MO, USA). The Cell Counting Kit (CCK-8) was bought from Jiangsu Aidisheng Biotechnology Co., Ltd. (Jiangsu, China). Indocyanine green (ICG) and dimethyl sulfoxide (DMSO) were purchased from Aladdin (Shanghai, China). 4′,6-Diamidino-2-phenylindole (DAPI) was bought from Beyotime (Shanghai, China). The live/dead staining kit was obtained from Yeasen Corporation (Shanghai, China). 2′,7′-Dichloro-fluorescein diacetate (DCFH-DA), filipin and dynasore were purchased from Yuanye Biological Technology (Shanghai, China).

2.2. Synthesis of MnAs-ICG

MnAs nanofiber was synthesized using a hydrothermal method. Briefly, $HAsNa_2O_4 \cdot 7H_2O$ solution (1.2 mmol) was mixed with $MnCl_2 \cdot 4H_2O$ solution (0.3 mmol) and stirred vigorously at 4 °C for 30 min, and then transferred to a stainless steel Teflon-lined autoclave at 180 °C for 30 min. The obtained MnAs was collected by centrifugation, washed, and redispersed in water.

To synthesize MnAs-ICG, ICG (2.6 mg) pre-dissolved in 300 μL of DMSO was added to 3 mL of MnAs solution under stirring overnight. The mixture was dialyzed against deionized water using a dialysis bag (MWCO = 3500 Da), and the products were stored at 4 °C.

2.3. Characterization of MnAs-ICG

The morphology, elemental mapping and energy dispersive X-ray spectroscopy (EDS) spectra of MnAs-ICG were observed using transmission electron microscopy (TEM) (FEI, Tecnai F20, Oregon, USA). And the surface morphology was observed using scanning electron microscopy (SEM) (Zeiss, Sigma 300, Oberkochen, Germany). The hydrodynamic diameter and zeta potential of MnAs-ICG were investigated using a Zetasizer (Malvern, Nano-ZS90, Worcestershire, UK). The amount of Mn and As was investigated by inductively coupled plasma mass spectrometry (ICP-MS, Thermo Electron Corporation, ICAP-QC, Waltham, MA, USA). ICG drug loading (DL) and encapsulation efficiency (EE) were determined by measuring ICG absorbance at 780 nm *via* a UV–Vis spectrometer (Molecular Devices, SpectraMax M2, Sunnyvale, CA, USA) and comparing them to standard curves of the free ICG. The DL and EE were calculated based on formulas, as shown in Eqs. (1) and (2). The valence of arsenic was evaluated using Atomic Fluorescence Spectroscopy (AFS, Shimadzu, Japan).

$$\mathrm{DL}(\%) = \frac{\text{Weight of loaded drug}}{\text{Total weight of NPs}} \times 100 \quad (1)$$

$$\mathrm{EE}(\%) = \frac{\text{Weight of loaded drug}}{\text{Total weight of feeding drug}} \times 100 \quad (2)$$

2.4. Computational methods

Molecular dynamics (MD) simulations were conducted to study Mn^{2+}, AsO_4^{3-}, and ICG behavior. The simulation calculation was conducted on four structures with an integration time-step of 1 fs. First, the conjugate gradient algorithm and energy minimization were performed to obtain a stable structure. Each sample was then equilibrated under the NPT ensemble at a constant temperature of 300 K to achieve an equilibrium state with zero pressure for 20 ns. Furthermore, a potential cutoff radius of 2.25 nm is applied in the calculation of the non-bonded interaction. Finally, the properties of the structures were obtained in the last 3000 ps. The interaction energy was calculated for measuring the interaction intensity between the Mn^{2+}, AsO_4^{3-}, and ICG.

2.5. *In vitro photothermal effect*

The temperature changes of MnAs-ICG of various concentrations were recorded to investigate the photothermal effect using an infrared (IR) thermal camera (Infrared Camera Inc., ICI 7320, Beaumont, TX, USA) under 808-nm laser irradiation.

2.6. *Quantitative analysis of ·OH generation*

·OH level was quantified using an electron spin resonance (ESR) spectrometer using DMPO as a spin trap. Briefly, MnAs-ICG at various pH conditions (7.4 or 5.0), 100 μL of H_2O_2 (2 mmol/L), and 40 μL of DMPO solution (0.5 mol/L) were instantly added to a capillary tube. The characteristic peak signals of ·OH were detected using an ESR spectrometer (Bruker, A300, Billerica, Germany).

2.7. *Hemolysis assay*

The hemolysis assay of MnAs-ICG was carried out on fresh blood from a New Zealand white rabbit. Briefly, 0.2 mL of fresh blood was collected, centrifuged (1500 rpm, 5 min, Thermo, Sorvall Legend Micro 17R, Lower Saxony, Germany), and washed with PBS. After dilution to 2% (*v*/*v*) with PBS, equal volume of red blood cells (RBCs) suspension and MnAs-ICG at various ICG concentrations (1, 2.5, 5, 8, 10 and 20 μg/mL) were mixed, and incubated at 37 °C for 1 h. After centrifugation (1500 rpm, 10 min, Thermo), the absorbance of supernatant at 414 nm was determined using microplate reader to calculate hemolysis rates.

2.8. *pH-Responsive study*

The pH-responsive characteristics of the MnAs-ICG nanospike were evaluated using TEM and *in vitro* release in PBS buffer at different pH conditions. First, MnAs-ICG was added to PBS at pH 6.2 and 5.0. At the selected time, the solution was collected for observation of morphological changes using TEM. Then, the release of ICG and As from MnAs-ICG at different pH values and photothermal treatments was measured by dialysis bag. Briefly, MnAs-ICG (ICG: 100 μg) was suspended in a dialysis bag (MWCO = 3500 Da), immersed in 10 mL of PBS (pH 7.4, 6.2, or 5.0), and incubated at 37 °C with constant stirring. Then, 1 mL of PBS was collected at specific time intervals, and the released As and ICG was measured according to the standard curve of As and ICG using ICP-MS (Thermo Electron Corporation) and UV−Vis spectrometer (Molecular Devices), respectively.

2.9. *3D tumor spheroids study*

4T1 cells (ATCC, 1×10^4) were incubated into ultralow attachment plates. After 3 days, tumor cell spheroids (~300 μm) were treated with fresh medium of various pH conditions (pH 7.4 or 6.2) containing MnAs-ICG (ICG: 25 μg/mL) for 12 h. After 4-h incubation, tumor cell spheroids of the laser treatment group were treated with an 808-nm laser (1 W/cm^2, 5 min) per well, followed by observation with confocal laser scanning microscope (CLSM, Zeiss, LSM880, Oberkochen, Germany).

2.10. *In vitro cellular uptake study*

4T1 cells were seeded into glass-bottom confocal dishes and treated with PBS or MnAs-ICG (ICG: 20 μg/mL) for 4 h. Two hours after laser irradiation, cells were washed and fixed with 4% paraformaldehyde, followed by DAPI staining and CLSM imaging (Zeiss).

2.11. *Internalization mechanism of cellular uptake*

To investigate the internalization mechanism of the MnAs-ICG, 2×10^5 of 4T1 cells were seeded into glass-bottom confocal dishes, and pre-incubated with Hank's, amiloride hydrochloride (30 μg/mL), chlorpromazine hydrochloride (10 μg/mL), dynasore (27.2 μg/mL) or filipin (5 μg/mL) for 30 min. After washed with PBS, cells were incubated with MnAs-ICG (ICG: 20 μg/mL) for 1 h. Then, the cells were fixed with paraformaldehyde and stained with DAPI for CLSM imaging (Zeiss). The 4 °C-treated group was incubated in 4 °C refrigerator.

2.12. *Reactive oxygen species (ROS) detection*

Cells (2×10^5) were seeded into confocal dishes. After incubation with PBS or MnAs-ICG (Mn: 20 μg/mL) for 6 h, the irradiated groups were deal with an 808-nm laser (1 W/cm^2, 5 min). After DCFH-DA (10 μmol/L) staining, cells were washed and observed using CLSM (Zeiss).

2.13. *In vitro cytotoxicity assay*

PTT/CDT/chemotherapy synergistic therapy of MnAs or MnAs-ICG was evaluated by CCK-8 assay. Briefly, 1×10^4 of 4T1 cells were seeded into 96-well plates and incubated with $MnCl_2$, $HAsNa_2O_4 \cdot 7H_2O$, ICG, MnAs or MnAs-ICG of different concentrations for 24 h. The irradiated groups were exposed to an 808-nm laser (1 W/cm^2, 5 min).

2.14. *Live/dead staining assay*

4T1 cells were seeded into culture dishes and incubated overnight, followed by incubation with PBS or MnAs-ICG (ICG: 20 μg/mL) for 4 h. After 2 h of incubation, the irradiation groups were irradiated for 5 min, followed by washing and co-staining with Calcein-AM and PI for 30 min. After PBS washing, cells were imaged using CLSM (Zeiss).

2.15. *Cell apoptosis assay*

4T1 cells were seeded into 6-well plates and treated with PBS or MnAs-ICG (ICG: 20 μg/mL). Four hours later, cells were irradiated for 5 min. After another 2-h incubation, cells were collected, washed, and co-stained with Annexin-FITC and PI for 15 min for flow cytometry (Beckman, CytoFlex, California, USA).

2.16. *In vivo pharmacokinetic study*

Male Sprague-Dawley (SD) rats (200 ± 15 g) were obtained from Zhejiang Chinese Medical University Laboratory Animal Research Center. All animal experiments were performed in compliance with guidance of the Zhejiang Chinese Medical University Animal Care and Use Committee. SD rats were randomly divided into two groups ($n = 3$), and intravenously injected with free ICG and MnAs-ICG (ICG: 1.5 mg/kg). The blood samples were obtained from retro-orbital plexus at selected times. After centrifugation and precipitation, the ICG concentration in plasma supernatant was measured *via* UV−Vis

spectrometer at 780 nm. And the pharmacokinetic parameters of ICG and MnAs-ICG were analyzed *via* PKSolver 2.0 (China Pharmaceutical University, China).

2.17. *In vivo imaging and ex vivo distribution analysis*

Female BALB/c mice (4−6 weeks, 20 ± 2 g) were obtained from Zhejiang Chinese Medical University Laboratory Animal Research Center. To prepare 4T1 tumor-bearing mice, 4T1 cells in PBS buffer were subcutaneously injected to the right back of mice at a dose of 1×10^6 per mouse. After 15 days, the mice could be used for *in vivo* experiments once the tumor volumes exceeded 100 mm^3. Mice were injected with ICG or MnAs-ICG (ICG: 2 mg/kg) *via* tail vein. At specified times (0.5, 1, 2, 5, 8, and 24 h), an *in vivo* imaging system was used to investigate the ICG fluorescence (excitation: 710 nm, filter: 745 nm; IVIS, PerkinElmer, Waltham, MA, USA). After 24-h post-injection, mice were sacrificed, and the major organs (heart, liver, spleen, lung, and kidney) and tumors were harvested for *ex vivo* imaging.

2.18. *MR imaging of MnAs-ICG*

For *in vitro* experiments, MnAs-ICG in PBS (pH 7.4 and 5.0) at various Mn concentrations for 24 h was scanned using the 1.5T MRI system (GE Healthcare, GE Signa HDxT, Little Chalfont, UK) to measure the T_1 relaxation time.

For *in vivo* experiments, MnAs-ICG was intravenously injected into mice (Mn: 1.25 mg/kg). *In vivo* T_1-weighted MRI images were obtained at selected times using a 1.5T MRI system (GE Healthcare).

2.19. *In vivo anti-tumor evaluation*

4T1 tumor-bearing mice of five groups were intravenously injected with saline, ICG, or MnAs-ICG (ICG: 2.5 mg/kg) ($n = 5$). After 5 h, the illumination groups were treated with laser irradiation (808 nm, 1 W/cm^2, 10 min). During this process, the temperature change of tumor site at different time points was monitored *via* an IR thermal imaging camera. During 21 days treatment period, body weight, tumor volume, and survival ratio were recorded every two days. Tumor volume was measured according to Eq. (3):

$$\text{Tumor volume} = \frac{\text{Tumor length} \times \text{Tumor width}^2}{2} \tag{3}$$

2.20. *Histopathology analysis*

Mice were sacrificed after 21 days, and the major organs and tumors were collected and fixed in 10% paraformaldehyde. After embedding in paraffin and sectioning, samples were stained with hematoxylin and eosin (H&E). The tumors were stained with terminal deoxynucleotidyl transferase-mediated nick end labeling (TUNEL).

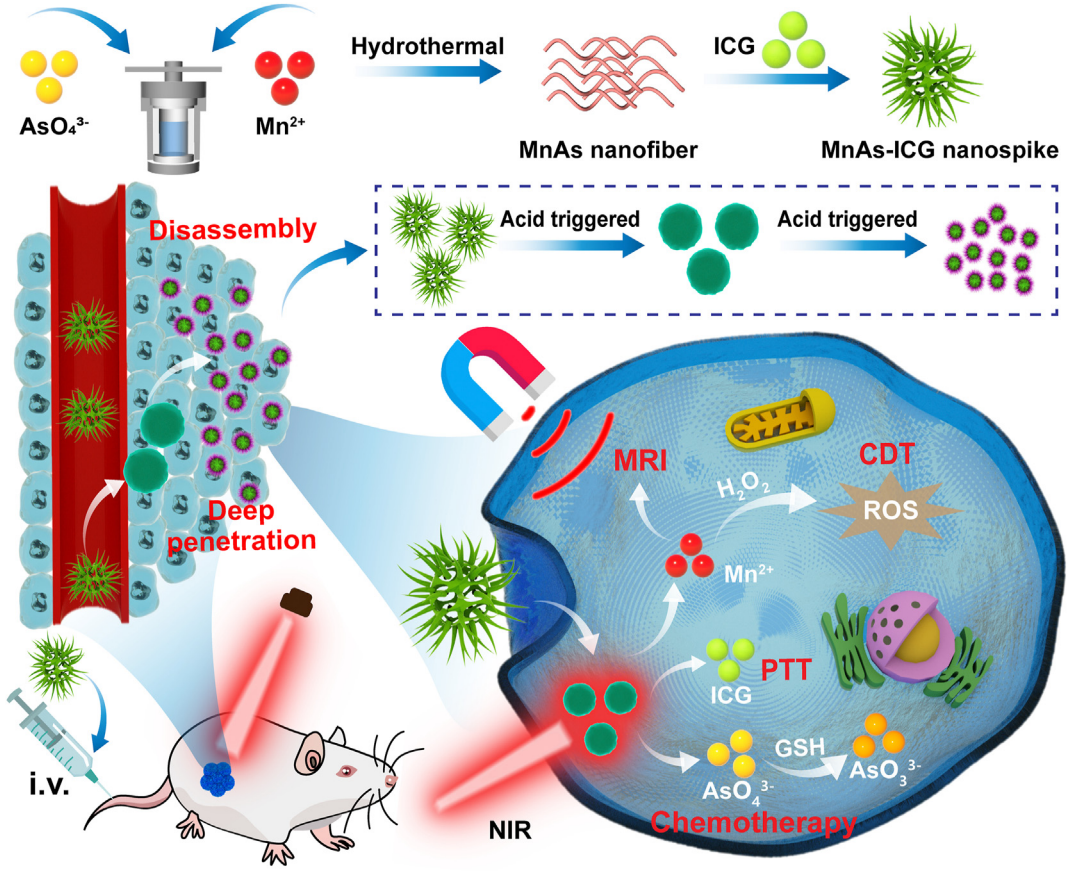

Figure 1 Schematic illustration of MnAs nanofiber and MnAs-ICG nanospike preparation, and pH-sensitive morphological transformation-enabled deep penetration and MRI and FL bimodal imaging-guided synergistic therapy.

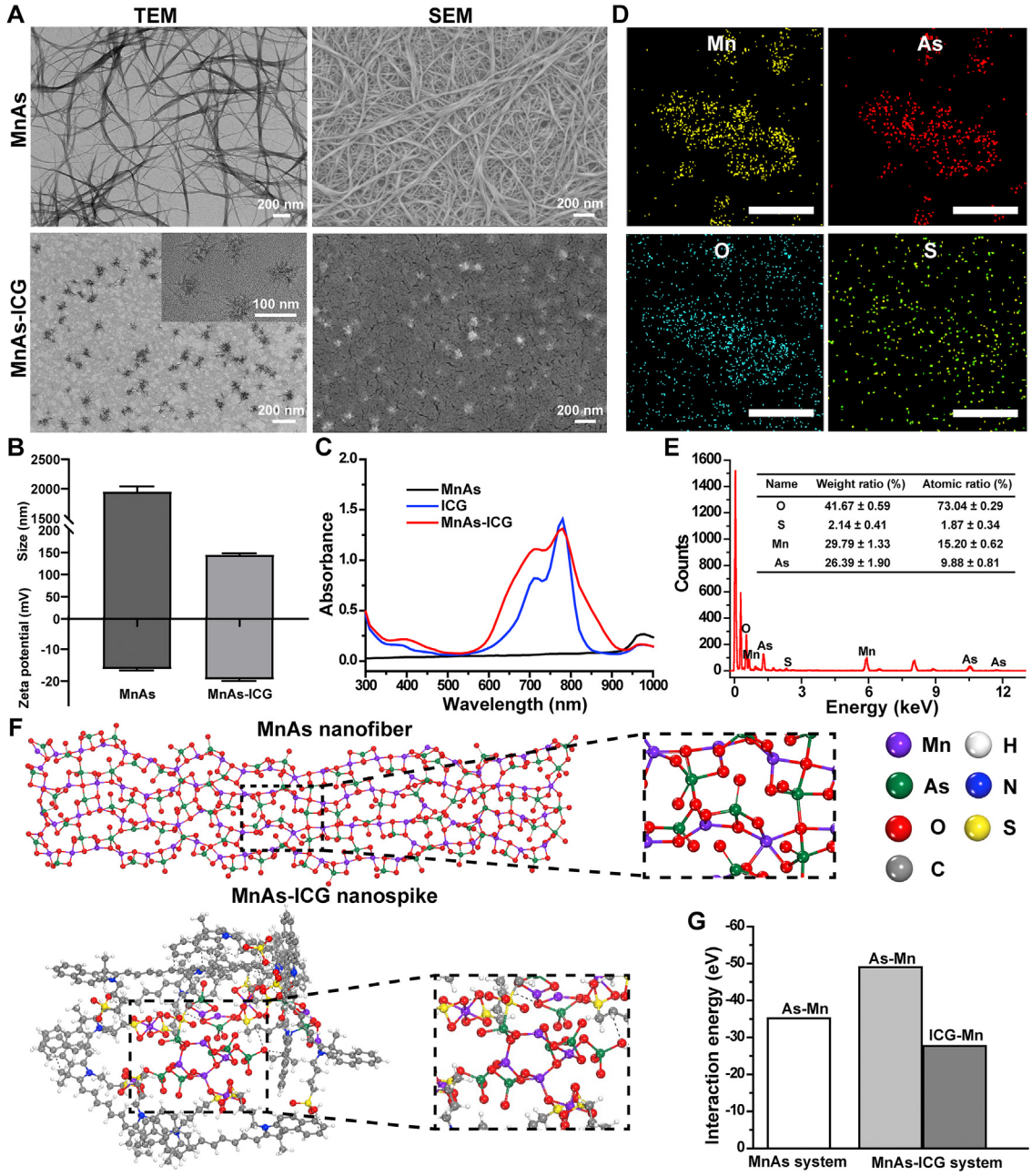

Figure 2 Characterization of MnAs nanofiber and MnAs-ICG nanospike. (A) TEM and SEM images of MnAs and MnAs-ICG. (B) Hydrodynamic diameter and zeta potential of MnAs and MnAs-ICG. Data are presented as mean ± SD ($n = 3$). (C) UV−Vis absorption spectra of MnAs, ICG and MnAs-ICG. (D) Elemental mapping and (E) EDS spectrum of MnAs-ICG. Scale bar = 100 nm. (F) MD simulation and (G) interaction energy of MnAs nanofiber and MnAs-ICG nanospike. The covalent interactions were marked by dashed line.

2.21. Statistical analysis

All data were presented as the mean ± standard deviation (SD) and analyzed using SPSS 25 (IBM SPSS Inc., Chicago, IL, USA). Statistical significance was set at $P < 0.05$, and $P < 0.01$ was considered as extreme significant.

3. Results and discussions

3.1. Design and preparations

GSH and ROS play critical roles in cancer-related redox homeostasis regulation. GSH depletion and ROS elevation would be

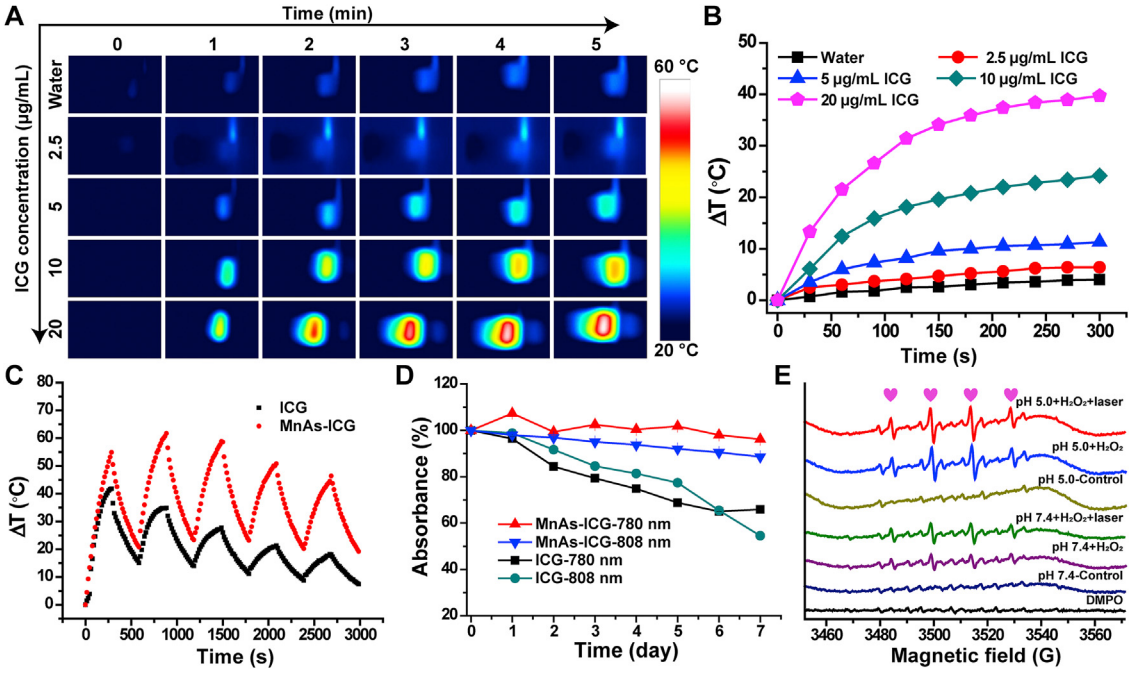

Figure 3 Photothermal conversion and ·OH generation. (A) Photothermal images and (B) corresponding temperature variation curve of MnAs-ICG with various ICG concentrations under 808-nm laser irradiation. (C) Photothermal stability of ICG and MnAs-ICG undergoing five rounds of laser irradiation. (D) The dynamic stability of ICG and MnAs-ICG at 4 °C, and calculated at 780 and 808 nm for ICG. (E) ESR spectra of ·OH generation under different conditions.

promising strategies for breast cancer treatment. As illustrated in Fig. 1, MnAs-ICG nanospike was constructed *via* a two-step process. First, Mn^{2+} (0.3 mmol) and AsO_4^{3-} (1.2 mmol) were mixed and complexed through electrostatic interaction, and colloidal suspension MnAs nanofiber was obtained *via* a hydrothermal method. Second, MnAs-ICG nanospike was formed when ICG self-assembled with MnAs nanofiber by competitive coordination interaction between Mn^{2+} and the two sulfonate anions of ICG. The as-obtained "all-in-one" nano-platform (MnAs-ICG nanospike) could combine the CDT of Mn^{2+}, chemotherapy of AsO_4^{3-} and PTT of ICG. Under the higher GSH level in TME, AsO_4^{3-} would deplete or exhaust GSH and be transformed to more toxic AsO_3^{3-}, further disturbing the balance between ROS and GSH to increase the intracellular ROS level and facilitating the CDT of Mn^{2+}. And ICG encapsulation *via* coordination interaction could not only improve the dynamic stability of ICG, but also enhance its *in vivo* circulation time. The prepared MnAs-ICG nanospike exhibited enhanced tumor accumulation and acid-responsive morphological transformation and dimensional variability, efficiently promoting deep tumor penetration for improved tumor therapy. Moreover, the photothermal ability of the nanospike could efficiently cooperate with chemotherapy and chemodynamic therapy in a multifunctional MRI-guided synergistic therapy for breast cancer treatment.

3.2. *Characterization of MnAs-ICG nanospike*

Transmission electron microscopy (TEM) and scanning electron microscopy (SEM) were employed to monitor the morphologies of MnAs and MnAs-ICG. Firstly, we investigated the formation of MnAs nanofiber *via* TEM. As shown in Supporting Information Fig. S1A, with the increasing of AsO_4^{3-}, MnAs showed obvious nanofiber-like morphology. Compared with the ratio of 1:1 or 1:2, MnAs at the ratio of 1:4 exhibited more uniform structure, hence 1:4 was chosen for further evaluation (Fig. 2A). As shown in Supporting Information Fig. S1B, the addition of ICG obviously changed the nanofiber-like morphology of MnAs, and led to a morphological transformation from the nanofiber of MnAs into a nanospike structure of MnAs-ICG, and more ICG would promote the formation of nanospike structure, which allowing for a more intact interaction with cells than a spherical structure[49]. And the results of dynamic light scattering (DLS) displayed that the hydrodynamic diameters of MnAs and MnAs-ICG were 1954.33 ± 87.08 nm and 144.87 ± 2.91 nm, respectively, which were in accordance with TEM results (Fig. 2B). In addition, compared to the MnAs nanofiber, the MnAs-ICG nanospike was negatively charged and displayed a slight decrease in zeta potential. And the molecular mass of MnAs-ICG was 229 kDa measured *via* Litesizer™ 500 (Anton Paar, Austria). The stability of MnAs-ICG nanospike in PBS (pH 7.4), DMEM, and 10% FBS solution was also investigated *via* DLS. As shown in Supporting Information Fig. S2, MnAs-ICG nanospike in different physiological conditions were similar and the hydrodynamic diameter remains almost unchanged over 7 days, demonstrating that MnAs-ICG nanospike could maintain a relatively stable state in blood circulation. The UV−Vis spectra of MnAs-ICG were evaluated using a UV−Vis spectrometer. The characteristic absorbance peak of MnAs-ICG nanospike became broader and exhibited a higher absorbance at 808 nm than ICG, further guiding the MnAs-ICG for superior photothermal converting under 808-nm laser irradiation[50] (Fig. 2C). Elemental mapping and energy dispersive X-ray spectroscopy (EDS) displayed uniform distribution of Mn, As, O, and S elements of MnAs-ICG with a weight ratio of 29.79 ± 1.33%, 26.39 ± 1.90%, 41.67 ± 0.59% and

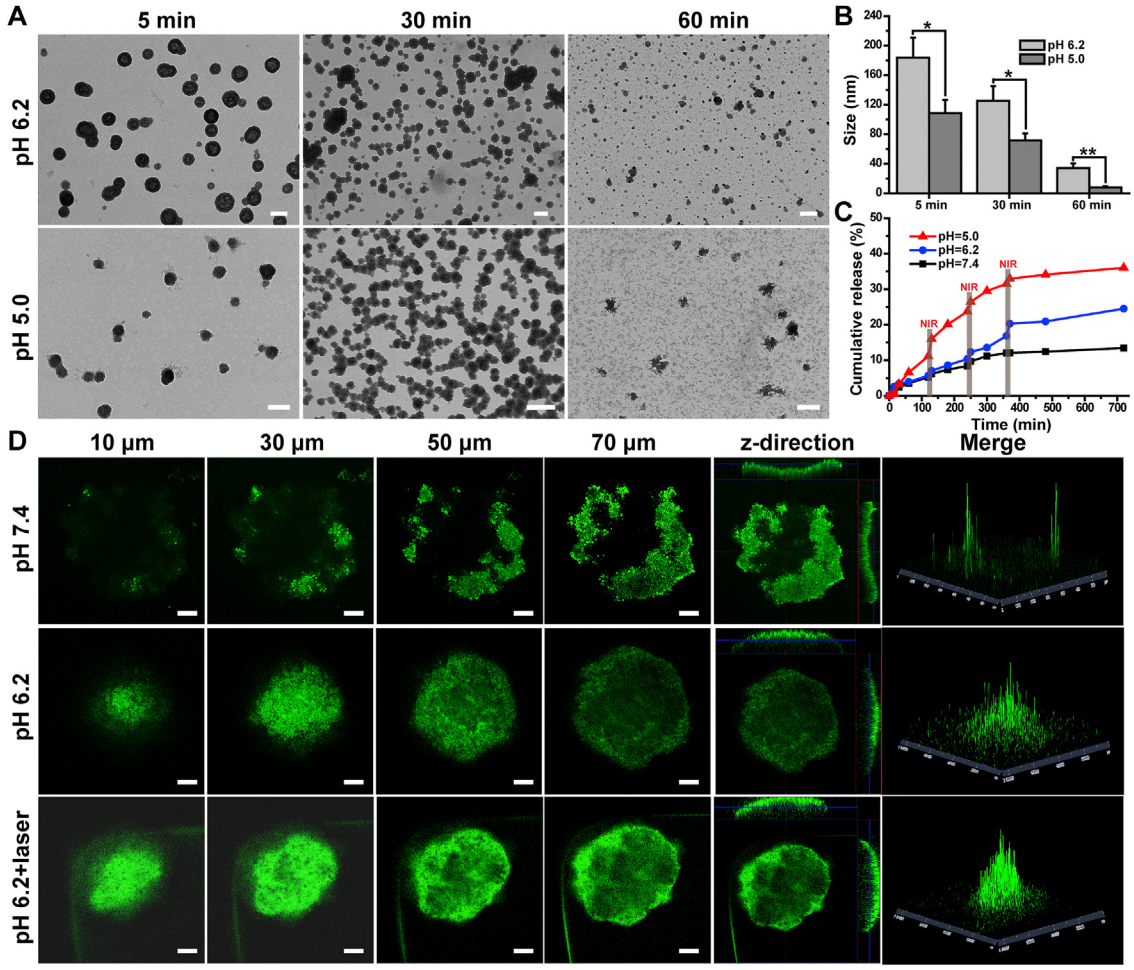

Figure 4 pH-responsive study. (A) The morphology and (B) size variation of MnAs-ICG at pH 6.2 and 5.0. Data are presented as mean ± SD ($n = 3$). Scale bar = 200 nm. (C) Cumulative release of ICG from MnAs-ICG at various conditions (pH 7.4, 6.2 or 5.0). (D) CLSM images of 3D tumor spheroids with different treatment. Scale bar = 100 μm $^{*}P < 0.05$, $^{**}P < 0.01$.

2.14 ± 0.41%, respectively (Fig. 2D and E). And the loading capacity and encapsulation efficiency of ICG in MnAs-ICG nanospike were 53.24 ± 3.66% and 65.75 ± 4.52%, respectively, further illustrating the high loading capacity of carrier-free nanodrugs. About 90.6% As (III) was converted from As (V) in MnAs-ICG under excessive GSH, which further demonstrated the reducibility of GSH on As (V).

Computational simulation by molecular dynamics (MD) was conducted to further explain the morphological transformation based on the hypothesis that the filamentous structures of MnAs nanofiber and the nanospike structures of MnAs-ICG were formed by multiple non-covalent interactions. Electrostatic self-assembly was mediated by electrostatic interactions between Mn^{2+} and AsO_4^{3-}, generating a self-confined effect for an organized arrangement of ionic groups aligned in the linear direction. Subsequently, owing to the higher interaction energy of ICG-Mn (−27.66 eV) than that of Mn-As (−35.16 eV), ICG competitively coordinated with the Mn^{2+} *via* coordination interaction, thereby breaking the nanofiber into small fractions, which then re-self-assembled into nanospike (Fig. 2F and G).

In order to confirm the photothermal potency of MnAs-ICG in PTT, we compared the photothermal effects of MnAs-ICG at various concentrations using 808-nm laser irradiation. MnAs-ICG nanospike exhibited a concentration-dependent temperature changing behavior, and the temperature change reached up to 39.7 °C at 20 μg/mL of ICG after 5 min of laser irradiation (Fig. 3A and B). Subsequently, the photothermal stability of MnAs-ICG was investigated using free ICG as a control. Compared to ICG, MnAs-ICG maintained good photothermal cycling stability after five rounds of 808-nm laser irradiation, effectively overcoming the shortage of easy photobleaching of ICG due to the stabilizing effect provided by the cooperative coordination interaction[17] (Fig. 3C). Then, the dynamic stability of free ICG and MnAs-ICG at 780 and 808 nm was monitored over a span of 7 days. As displayed in Fig. 3D, the absorbance of ICG showed a noticeable attenuation of approximately 35% after 7 days at 4 °C. In contrast, MnAs-ICG showed a negligible change, suggesting excellent dynamic stability, which might be due to the coordination interaction between ICG and Mn^{2+}.

Electron spin resonance (ESR) was utilized to explore the •OH generation using DMPO as a spin trap. As shown in Fig. 3E, typical 1:2:2:1 multiple peaks were observed with co-existence of MnAs-ICG and H_2O_2. At pH 5.0, the multiple peaks of •OH were enhanced compared to those at pH 7.4, suggesting the pH-

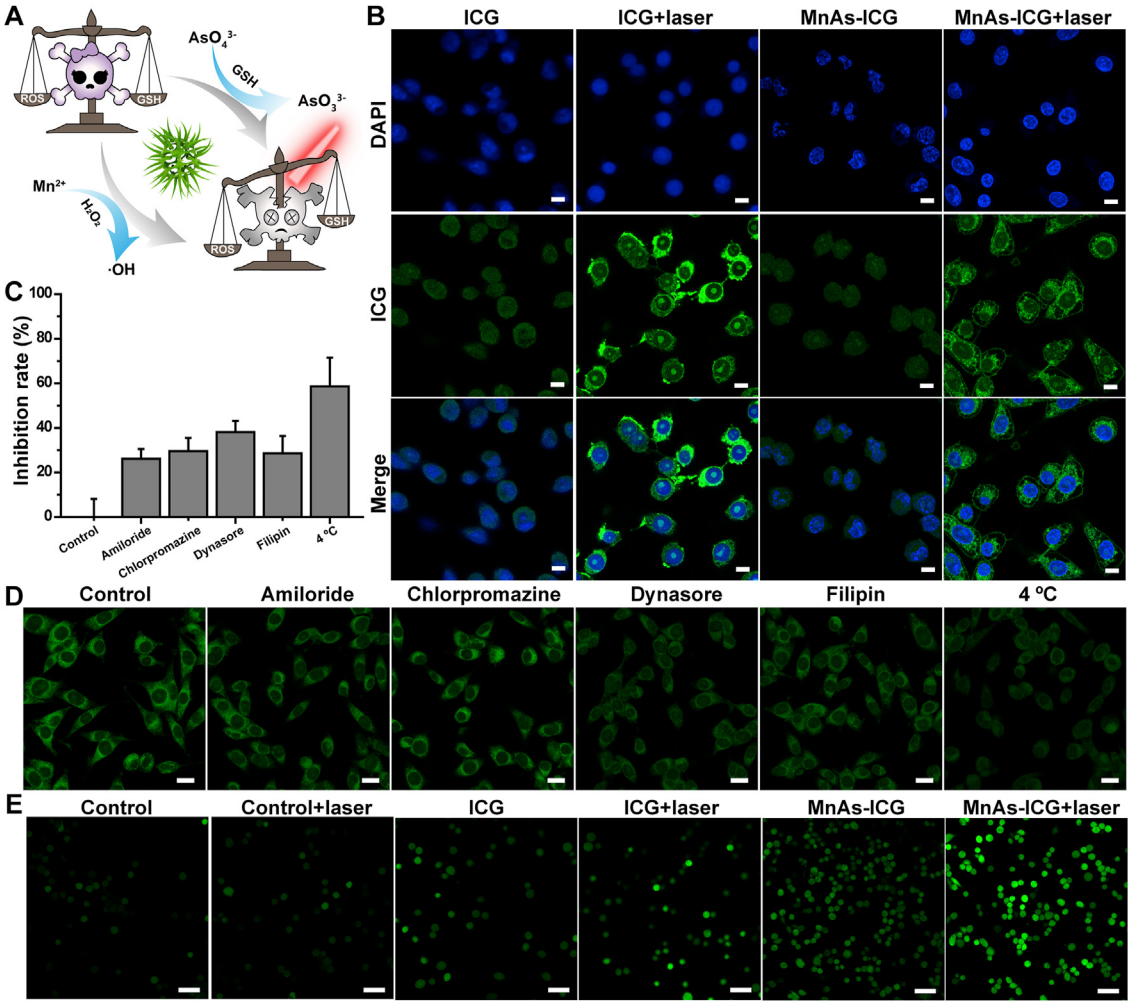

Figure 5 *In vitro* cellular uptake study. (A) Schematic illustration of the balance between ROS and GSH. (B) CLSM images of ICG and MnAs-ICG in 4T1 cells of different treatment. Scale bar = 10 μm. (D) CLSM images and (C) its corresponding inhibition rate of ICG and MnAs-ICG internalized by 4T1 cells treated with PBS, amiloride (macropinocytosis inhibitor), chlorpromazine (clathrin inhibitor), dynasore (caveolae/clathrin inhibitor), filipin (caveolae inhibitor) at 37 °C, and PBS at 4 °C (inhibition of ATP-mediated endocytosis). Scale bar = 20 μm. (E) Intracellular ROS detections after PBS, ICG or MnAs-ICG treatment. Scale bar = 50 μm.

responsive properties of MnAs-ICG for increased oxidative stress. In addition, 808-nm laser irradiation further enhanced the generation of ·OH *via* the boosting effect of hyperthermia.

3.3. *pH-Responsive study*

Based on the pH-sensitivity of MnAs as previously reported[41,42], TEM was used to investigate the morphological transition of the MnAs-ICG nanospike after incubation in PBS at pH 6.2 or 5.0 for various time periods. After 5-min incubation at pH 6.2, the nanospike collapsed and MnAs-ICG showed a hollow spherical nanostructure (Fig. 4A and B). At 30 min, MnAs-ICG partially decomposed into smaller nanoparticles of 34.26 ± 5.97 nm, allowing deep tumor penetration triggered by TME. As for pH 5.0, MnAs-ICG nanospike was almost degraded into ultra-small nanoparticles with the size of 7.83 ± 1.71 nm, which might be beneficial for on-demand release of functional therapeutic agents after cellular uptake.

The pH-sensitive cumulative drug release was determined using a dialysis method. At pH 7.4 for 12 h, the cumulative release of ICG was approximately 13.44% and increased significantly to 24.51% and 36.04% at pH 6.2 and 5.0, respectively. There were about 12.04% and 16.15% of As released from MnAs-ICG incubated in pH 7.4 and pH 6.2 PBS for 12 h, while up to 37.93% of As was released when the environmental pH was adjusted to 5.0, which is similar to the pH value of the tumor microenvironment, thus exhibiting a pH-sensitive release behavior (Fig. 4C and Supporting Information Fig. S3). In addition, the release of ICG was enhanced by laser irradiation at all pH conditions, suggesting a photothermal-assisted release property of MnAs-ICG.

Furthermore, 3D tumor spheroids were used to investigate the pH-sensitive penetration of MnAs-ICG. As shown in Fig. 4D, the fluorescence of ICG was mainly distributed at the edges of the spheroid after treatment with MnAs-ICG at pH 7.4. On the contrary, the fluorescence localized in the center of the 3D tumor spheroids at pH 6.2, indicating the excellent penetration of MnAs-ICG, which should be attributed to acid-triggered size variability.

With the combination of laser irradiation, the fluorescence was significantly enhanced in the center of tumor spheroids, benefiting from the photothermal effect-induced tumor-priming effect.

3.4. *In vitro cellular uptake study*

GSH and ROS are two main substances in cancer-related redox homeostasis regulation. Once disrupting the balance between them, the tumor cells would be damaged by the overproduction of ROS (Fig. 5A). It is essential for nanosystem-mediated cancer treatment to evaluate the cellular uptake efficiency. The subcellular localization of ICG in 4T1 cells was investigated *via* confocal laser scanning microscopy (CLSM). As displayed in Fig. 5B, ICG was mainly distributed in the cytoplasm due to the bonding action of ICG and intracellular glutathione *S*-transferase[51]. Notably, the FL signals of ICG increased significantly in 4T1 cells after 808-nm laser irradiation both in the group of ICG + laser and MnAs-ICG + laser, which could be explained by the hyperthermia caused by the laser. It has been reported that laser-induced hyperthermia can increase the permeability and fluidity of cell membrane, thereby facilitating cellular uptake to enhance drug endocytosis inside cancer cells and cause severe damage to the cells[51,52].

3.5. *Internalization mechanism of cellular uptake*

The internalization mechanism of MnAs-ICG nanospike was investigated *via* CLSM. Four inhibitors (amiloride, chlorpromazine, dynasore and filipin), and 4 °C-treatment were utilized to inhibit macropinocytosis-mediated, clathrin-mediated, caveolae/clathrin-mediated, caveolae-mediated and ATP-dependent endocytosis, respectively[53–55]. An obvious decrease in the fluorescence intensity was observed in the inhibitor and 4 °C-treatment groups, indicating that four inhibitors and 4 °C-treatment might be involved in endocytosis pathway (Fig. 5C and D and Supporting Information Fig. S4). While 4 °C-treatment group showed the lowest ICG fluorescence intensity and highest inhibition rate (58.7 ± 12.9%) compared to the control group, indicating that the internalization of MnAs-ICG mainly depends on ATP-mediated endocytosis pathway.

3.6. *Reactive oxygen species (ROS) detection*

Based on its green fluorescence generated *via* oxidization of DCFH-DA by ROS, dichlorofluorescein (DCF) was used to investigate the intracellular ROS production[56]. As displayed in Fig. 5E, evident fluorescence could be observed in cells incubated with MnAs-ICG for 6 h compared to the control group or ICG group with or without laser irradiation, which could be ascribed to the Mn^{2+}-mediated Fenton-like reaction. Upon 808-nm laser irradiation, the most potent green fluorescence was observed, indicating sufficient production of ·OH boosted by laser irradiation-induced temperature increase[15].

3.7. *In vitro synergistic therapy effect*

To visually observe live and dead cells, cells were co-stained with Calcein-AM and PI with live cells for green fluorescence and dead cells for red fluorescence[36]. As displayed in Fig. 6A and

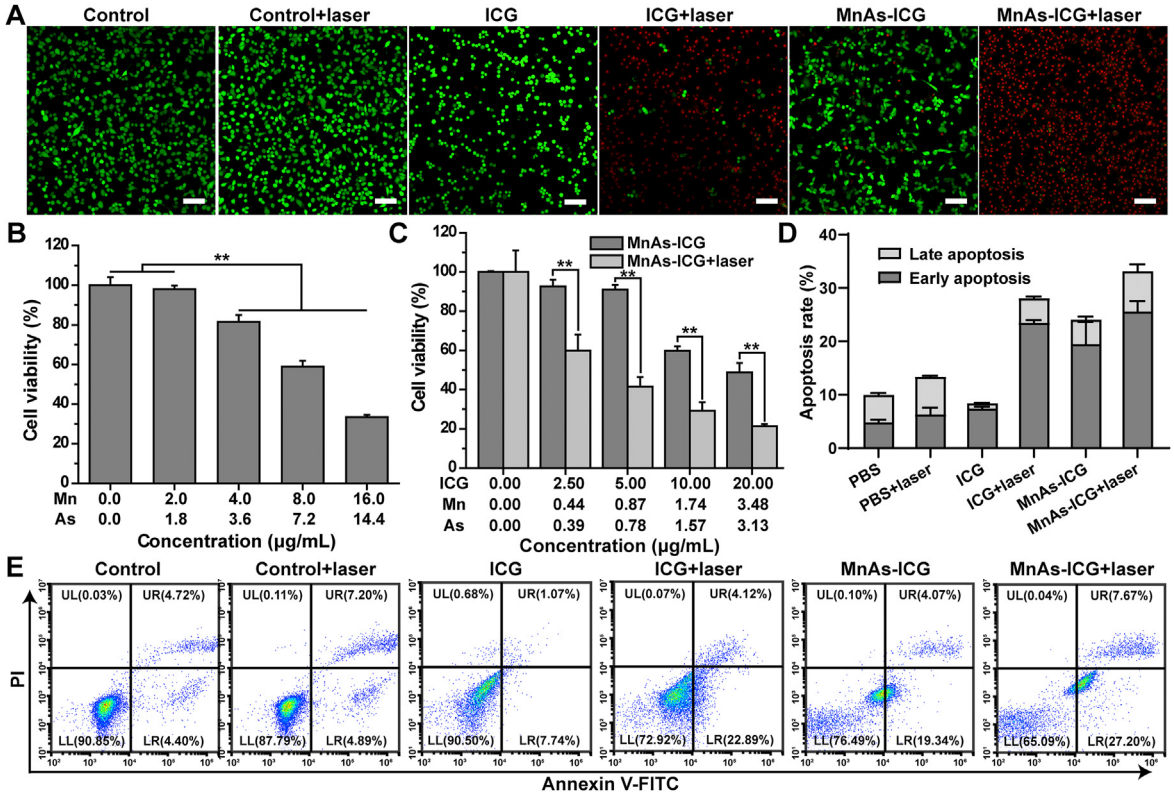

Figure 6 *In vitro* cytotoxicity study. (A) Live/dead staining assay after treatment with PBS, ICG or MnAs-ICG. Scale bar = 100 μm. Cell viability of 4T1 cells after treatment with (B) MnAs or (C) MnAs-ICG at various concentrations. Data are presented as mean ± SD (n = 6). (E) Cell apoptosis by flow cytometry and (D) its quantification after treatment with PBS, ICG or MnAs-ICG with or without laser irradiation. Data are presented as mean ± SD (n = 3). $^{**}P < 0.01$.

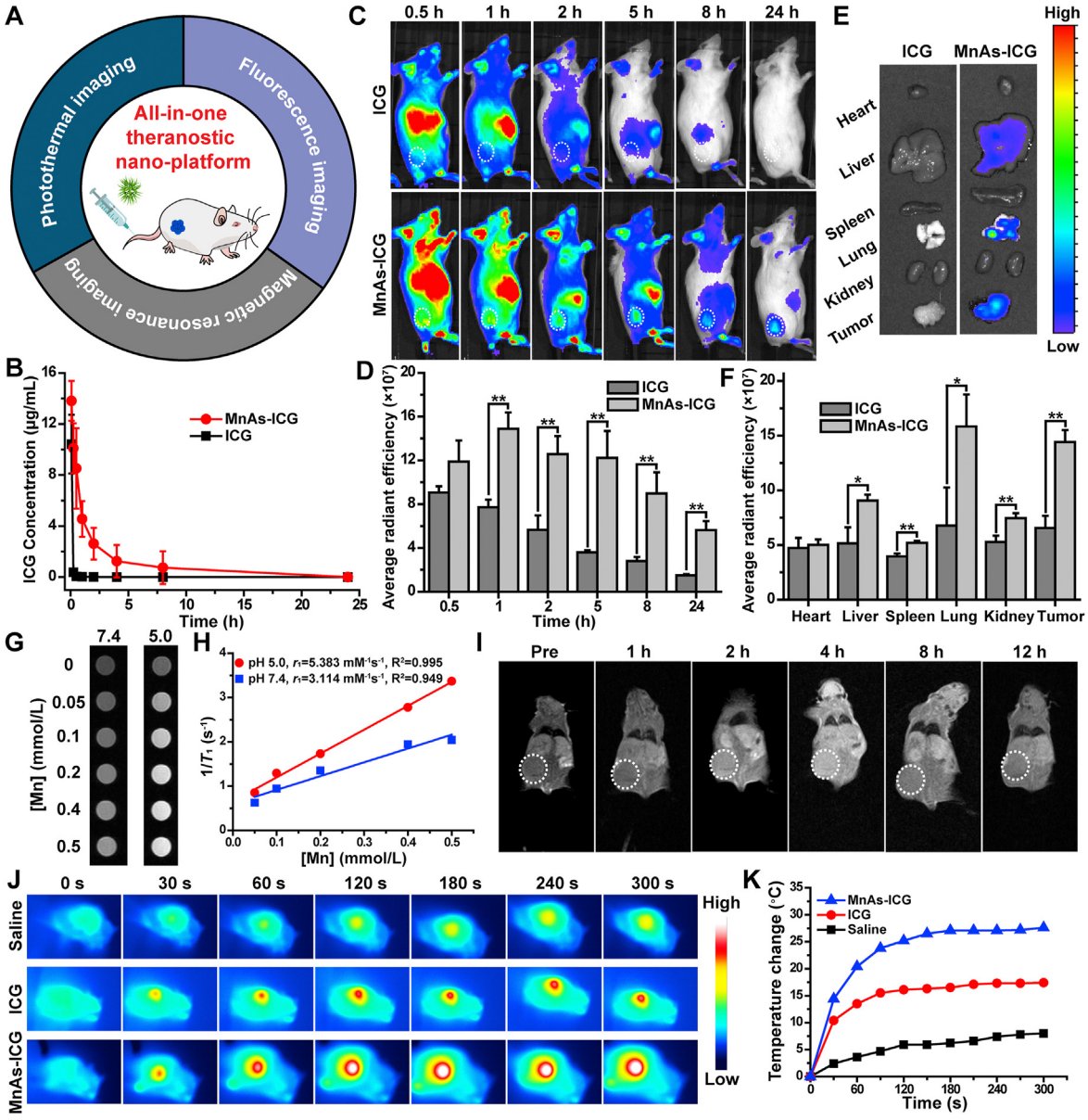

Figure 7 *In vivo* pharmacokinetic study, fluorescence, MRI and photothermal imaging. (A) Schematic illustration of *in vivo* applications of MnAs-ICG nanospike. (B) The pharmacokinetics profiles after ICG or MnAs-ICG treatment. Data are presented as mean ± SD ($n = 3$). (C) FL images of ICG or MnAs-ICG injected 4T1 tumor-bearing mice. (D) Semi-quantitative FL intensity of ICG around the tumors after ICG or MnAs-ICG treatment. Data are presented as mean ± SD ($n = 3$). (E) *Ex vivo* FL images of major organs and tumors at 24-h post-injection. (F) *Ex vivo* FL intensity of ICG or MnAs-ICG. Data are presented as mean ± SD ($n = 3$). (G) *In vitro* MRI images and (H) corresponding r_1 value of MnAs-ICG at various pH solution. (I) *In vivo* T_1-weighted MRI of mice at selected times after MnAs-ICG injection. (J) Infrared thermal images and (K) corresponding temperature change of 4T1 tumor-bearing mice at 5 h after saline, ICG or MnAs-ICG injection upon 808-nm laser irradiation. The tumor was marked by white dotted circles. $^*P < 0.05$, $^{**}P < 0.01$.

Supporting Information Fig. S5, cells did not show cell damage after treatment with PBS with or without laser irradiation and ICG. As for the MnAs-ICG groups, a small fraction of cells died because of the CDT effect of •OH mediated by Mn^{2+} and AsO_4^{3-} cytotoxicity. Following laser irradiation, robust red FL signals were observed after MnAs-ICG treatment, suggesting that the majority of 4T1 cells died after synergistic therapy treatment.

Based on the above results, *in vitro* synergistic therapy effect was investigated on 4T1 cells. To evaluate the cell viability of 4T1 cells treated by Mn^{2+}, AsO_4^{3-}, MnAs or MnAs-ICG of different conditions, CCK-8 assay was conducted, and the result showed that the cell viability decreased when concentration of MnAs increased, suggesting that the combination of chemotherapy with AsO_4^{3-} and CDT of Mn^{2+} had the potential to kill tumor cells (Fig. 6B and Supporting Information Fig. S6). After treatment with MnAs-ICG, 4T1 cell viability was also reduced with an increase in the ICG concentration (Fig. 6C). Furthermore, cellular activity dramatically decreased to 21.31 ± 1.10% after treatment with MnAs-ICG + 808-nm laser irradiation (ICG: 20 μg/mL), indicating the enhanced anti-tumor effect mediated by

Table 1 The main pharmacokinetic parameters of ICG after treatment with ICG or MnAs-ICG in SD rats.

Parameter	ICG	MnAs-ICG
$t_{1/2\beta}$ (min)	48.60 ± 6.10	147.73 ±133.62
CL [(μg)/(μg/mL)/min]	1.43 ± 0.57	0.24 ± 0.12*
AUC_{0-t} (μg/mL·min)	210.24 ± 91.31	1145.12 ± 518.13
MRT (min)	4.52 ± 1.22	192.54 ± 173.69
V_{ss} [μg/(μg/mL)]	7.15 ± 4.38	28.09 ± 9.67*

Data are presented as mean ± SD ($n = 3$). *$P < 0.05$ *vs.* ICG group.
$t_{1/2\beta}$, elimination half-life; CL, clearance rate; AUC, area under the curve; MRT, mean residence time; V_{ss}, volume of distribution.

photothermal effect of ICG, which further confirmed the adequate lethality on 4T1 cells achieved by the synergistic effect ($P < 0.01$).

After co-staining with Annexin V-FITC and PI, the apoptosis ratio of 4T1 cells after PBS or MnAs-ICG treatment with or without laser irradiation was analyzed using flow cytometry. As shown in Fig. 6D and E, 4T1 cells incubated with MnAs-ICG displayed a small amount of early apoptosis, and the control group exhibited relatively low apoptosis with or without laser irradiation. The MnAs-ICG + laser group showed the greatest fraction of cells undergoing early apoptosis as well as slight late apoptosis, highlighting the superior trimodal combination therapy achieved *in vitro*. Furthermore, the results of cell apoptosis were in line with the CCK-8 and live/dead assays.

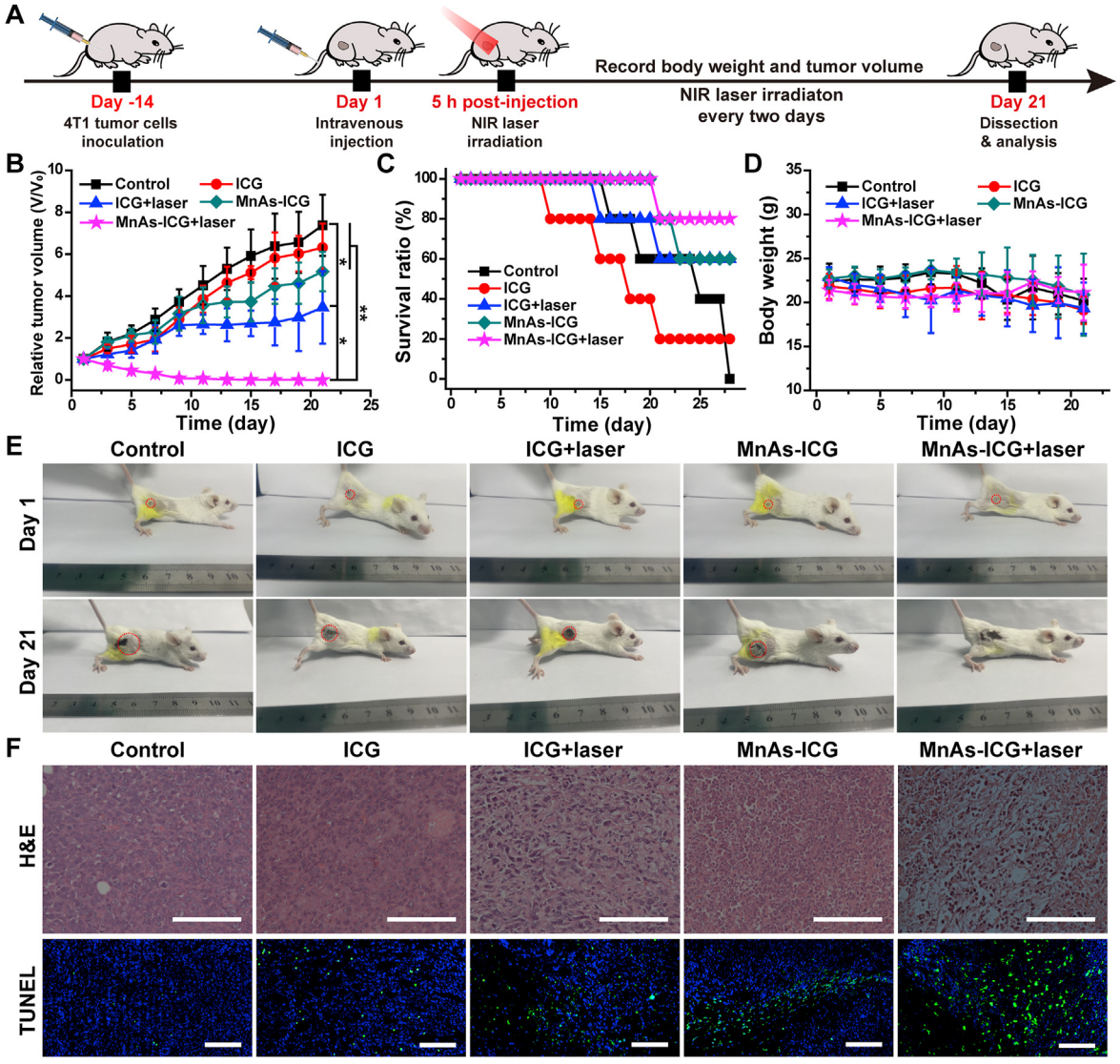

Figure 8 *In vivo* pharmacodynamics study. (A) Schematic illustration of the therapeutic protocol. (B) Relative tumor volume, (C) survival ratio and (D) body weight of mice after saline, ICG, ICG + laser, MnAs-ICG or MnAs-ICG + laser treatment. Data are presented as mean ± SD ($n = 5$). (E) Photographs of mice on Days 1 and 21. The tumor was marked by red dotted circles. (F) H&E and TUNEL staining of tumors. Scale bar = 100 μm. *$P < 0.05$, **$P < 0.01$.

3.8. *In vivo pharmacokinetic study*

In this study, MnAs-ICG nanospike was constructed as an "all-in-one" theranostic nano-platform, which could be applied in fluorescence imaging, MRI and photothermal imaging (Fig. 7A). Owning to its strong non-specific binding with plasma proteins, ICG, whose half-life is 3−4 min, is rapidly eliminated from the body after intravenous administration[57]. Normally, ICG is permanently entrapped or conjugated to nanoparticles for prolonging the *in vivo* circulation time. Hence, the pharmacokinetic profiles of ICG and MnAs-ICG were studied to investigate their blood circulation and retention time. As shown in Fig. 7B, free ICG was quickly removed from the circulating system at 5 min after administration, while MnAs-ICG exhibited a markedly delayed blood clearance. And the pharmacokinetic parameters showed that MnAs-ICG could significantly increase the area under the curve (AUC) from 210.24 ± 91.31 to 1145.12 ± 518.13 μg/mL·min, and prolonged $t_{1/2\beta}$ of ICG from 48.60 ± 6.10 to 147.73 ± 133.62 min, which was helpful for subsequent *in vivo* imaging and anti-tumor evaluation (Table 1).

3.9. *In vivo imaging and ex vivo distribution analysis*

We then investigated the *in vivo* real-time and *ex vivo* tumor and organs distribution of ICG or MnAs-ICG using the FL of ICG. The FL signals were extensively observed in the liver but less at the tumor site and completely extinguished at 24-h post-injection (Fig. 7C). In contrast, MnAs-ICG exhibited significantly enhanced FL signals with increased time intervals, peaked at 1 h after injection (Fig. 7D), then kept retaining at the tumor site over 24 h, confirming the enhanced specific tumor-targeting ability and prolonged circulation time ($P < 0.01$). At 24-h post-injection, *ex vivo* FL signals were further performed to assess the MnAs-ICG distribution in tumors and major organs. As displayed in Fig. 7E and F, FL signals could be clearly detected in the tumors of MnAs-ICG group, while no obvious FL signal could be observed in tumors or organs in the ICG group, further indicating the prolonged circulation time and enhanced tumor-targeting ability of MnAs-ICG. In addition, FL signals could also be observed in the liver and lung on account of the clearance effects of the reticuloendothelial system (RES).

3.10. *MR imaging of MnAs-ICG*

Once arriving at the tumor site, mild acidity of TME would decompose MnAs-ICG, and the released Mn^{2+} can be utilized for MRI. *In vitro* MRI results showed that the r_1 value of MnAs-ICG at pH 5.0 was significantly higher than that at pH 7.4 (Fig. 7G and H). For *in vivo* MRI experiments, mice were intravenously injected with MnAs-ICG and scanned using a 1.5T MRI system. As displayed in Fig. 7I, the MRI signals increased and peaked at 4 h, followed by a gradual decrease, well conforming to the FL imaging study. *In vitro* and *in vivo* MRI results suggested inspiring

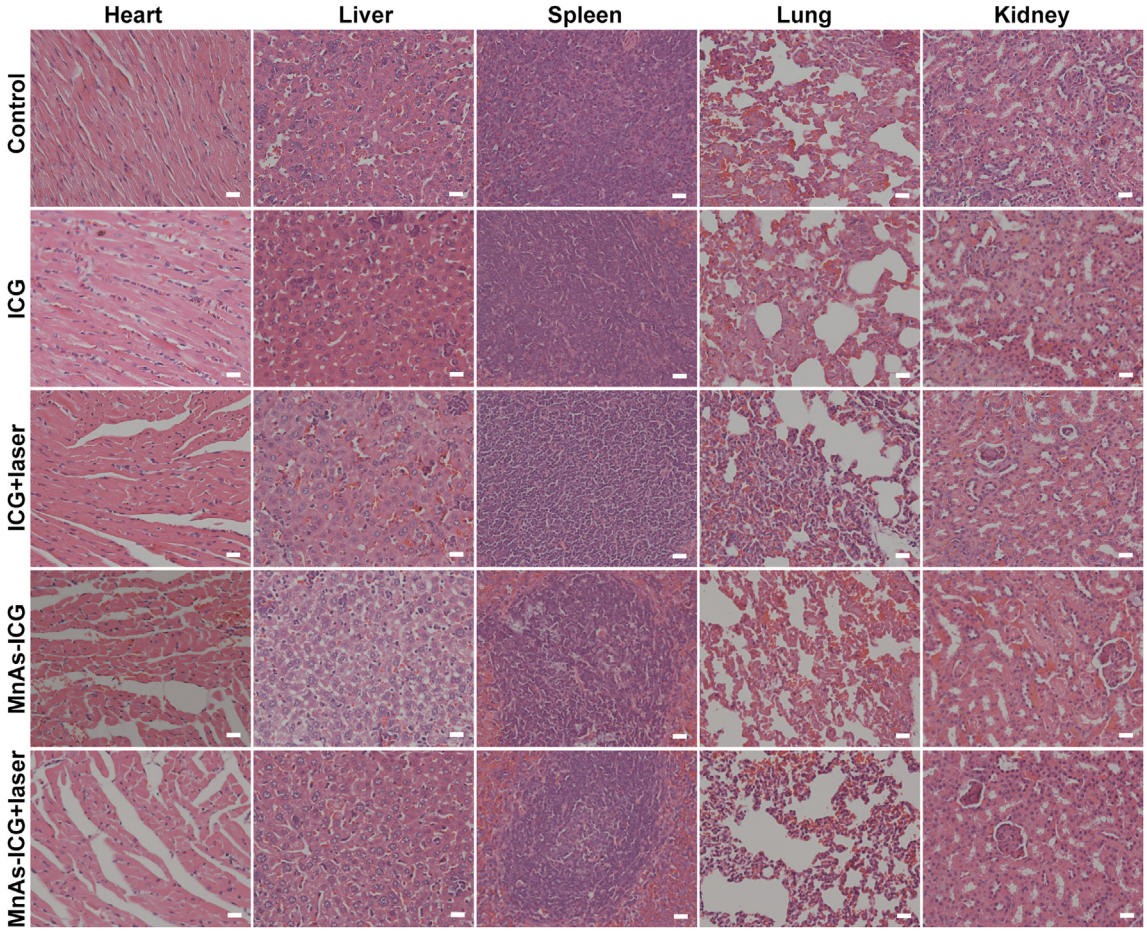

Figure 9 H&E staining of major organs after treatment with saline, ICG, ICG + laser, MnAs-ICG or MnAs-ICG + laser. Scale bar = 20 μm.

potential of MnAs-ICG to be an effective contrast agent for accurate tumor detection.

3.11. *In vivo photothermal imaging*

Encouraged by the superior photothermal ability of MnAs-ICG, *in vivo* photothermal imaging at the tumor site was performed to assess the photothermal conversion capability of MnAs-ICG. After intravenous administration of saline, ICG, or MnAs-ICG for 5 h, the temperature changes at the tumor site were recorded during irradiation. As displayed in Fig. 7J and K, temperature at the tumor site rapidly increased with 27.6 °C within 5-min irradiation, suggesting effective *in vivo* photothermal conversion and promising tumor killing ability of MnAs-ICG. Whereas the temperature of mice intravenously injected with free ICG increased by 17.4 °C with 5-min laser irradiation, which might be caused by the relatively insufficient tumor accumulation and poor photostability of free ICG[58].

3.12. *In vivo anti-tumor study*

To further assess the combined anti-tumor efficiency of chemodynamic therapy, chemotherapy and photothermal therapy induced by MnAs-ICG, *in vivo* anti-tumor study was conducted with 4T1 tumor-bearing mice. Schematic illustration of experimental protocol is shown in Fig. 8A. During a 21-day treatment period, the tumor volume of mice treated with saline or ICG increased rapidly, while that of mice receiving MnAs-ICG treatment showed a certain inhibitory effect owing to the synergistic therapy of MnAs-ICG (Fig. 8B and E). Compared with ICG + laser group, the mice treated with MnAs-ICG + 808-nm laser irradiation showed excellent inhibition effect on tumors, and the tumors were negligible since Day 9. Mice treated with MnAs-ICG + laser resulted in the highest survival ratio during a 28-day period, while no mice survived after Day 28 in the saline group (Fig. 8C). Body weight was used as an index for evaluation of *in vivo* cytotoxicity. The body weight of mice treated with saline, ICG, ICG + laser or MnAs-ICG treatment suffered a slight reduction, whereas the body weight of mice in the MnAs-ICG + laser group remained stable during the treatment period (Fig. 8D).

The *in vivo* anti-tumor effect of MnAs-ICG was further verified by H&E and TUNEL staining. Compared with that of other groups, tumor tissue treated with MnAs-ICG with 808-nm laser irradiation exhibited the most severe vacuolization and apoptotic characteristics (Fig. 8F). Furthermore, the cell apoptosis of tumors was observed *via* immunofluorescent TUNEL staining assay. As shown in Fig. 8F and Supporting Information Fig. S7, compared with other groups, the tumors of MnAs-ICG + laser displayed the most TUNEL-positive cancer cells, which indicated that MnAs-ICG with 808-nm laser irradiation showed the best anti-tumor effect.

Furthermore, the hemolysis assay showed that MnAs-ICG did not cause hemolysis of red blood cells (RBCs) with ICG concentrations as high as 20 μg/mL, indicating the excellent hemocompatibility and biosafety of MnAs-ICG (Supporting Information Fig. S8).

Moreover, no apparent damage was observed in the major organ tissues stained with H&E (Fig. 9). Overall, these results indicate that the synergistic therapy mediated by MnAs-ICG can significantly inhibit tumor growth with excellent *in vivo* biosafety.

4. Conclusions

In this study, MnAs-ICG nanospike was constructed as a multifunctional nano-platform for bimodal imaging-guided photothermal/chemo/chemodynamic synergistic therapy. The MnAs-ICG nanospike displayed excellent pH/photothermal dual-responsive release. In addition, the MnAs-ICG nanospike showed high photothermal conversion efficiency, which could efficiently improve the cellular uptake and cytotoxicity in 4T1 cells. Furthermore, *in vivo* FL and MR imaging results showed that MnAs-ICG could prolong the circulation time of ICG and enhance specific tumor-targeting potency. Finally, the *in vivo* anti-tumor in 4T1 tumor-bearing mice results showed that MnAs-ICG could efficiently inhibit tumor growth and had no apparent damage to normal tissues. In summary, MnAs-ICG may be utilized as an excellent nanomaterial for MRI-guided breast cancer treatment.

Acknowledgements

This work was supported by National Natural Science Foundation of China (81873014, 82074027, 81873018 and 82104405), Natural Science Foundation of Zhejiang Province (LZ21H280001 and LY21H280007, China), Zhejiang Chinese Medical University School-level Scientific Research Fund Project (2020ZG21, 2019ZG37, China), Traditional Chinese Medicine Science and Technology Plan of Zhejiang Province (2021ZQ036, China) and Jinhua Science and Technology Research Plan Project (2019-4-037, China). We appreciate the great help from the Public Platform of Medical Research Center, Academy of Chinese Medical Sciences, Zhejiang Chinese Medical University.

Author contributions

Hongyue Zheng, Fanzhu Li and Ji-Gang Piao designed the research. Xiaojie Chen and Xudong Fan carried out the experiments and performed data analysis. Yue Zhang participated part of the experiments. Yinghui Wei, Hangsheng Zheng, Dandan Bao and Hengwu Xu provided some suggestions. Xiaojie Chen and Ji-Gang Piao wrote the manuscript. Xiaojie Chen and Xudong Fan revised the manuscript. All of the authors have read and approved the final manuscript.

Conflicts of interest

The authors have no conflicts of interest to declare.

Appendix A. Supporting information

Supporting information to this article can be found online at https://doi.org/10.1016/j.apsb.2022.02.027.

References

1. Sung H, Ferlay J, Siegel RL, Laversanne M, Soerjomataram I, Jemal A, et al. Global cancer statistics 2020: GLOBOCAN estimates of incidence and mortality worldwide for 36 cancers in 185 countries. *CA Cancer J Clin* 2021;**71**:209–49.
2. Zhang H, Liu K, Li SK, Xin X, Yuan SL, Ma GH, et al. Self-assembled minimalist multifunctional theranostic nanoplatform for magnetic resonance imaging-guided tumor photodynamic therapy. *ACS Nano* 2018;**12**:8266–76.

3. Dong ZL, Gong H, Gao M, Zhu WW, Sun XQ, Feng LZ, et al. Polydopamine nanoparticles as a versatile molecular loading platform to enable imaging-guided cancer combination therapy. *Theranostics* 2016;**6**:1031−42.
4. Mei H, Cai SS, Huang D, Gao HL, Cao J, He B. Carrier-free nanodrugs with efficient drug delivery and release for cancer therapy: from intrinsic physicochemical properties to external modification. *Bioact Mater* 2021;**8**:220−40.
5. Qin Y, Tong F, Zhang W, Zhou Y, He SQ, Xie R, et al. Self-delivered supramolecular nanomedicine with transformable shape for ferrocene-amplified photodynamic therapy of breast cancer and bone metastases. *Adv Funct Mater* 2021;**31**:2104645.
6. Lin JF, Li C, Guo Y, Zou JJ, Wu PY, Liao YQ, et al. Carrier-free nanodrugs for *in vivo* NIR bioimaging and chemo-photothermal synergistic therapy. *J Mater Chem B* 2019;**7**:6914−23.
7. Huang L, Zhao SJ, Fang F, Xu T, Lan MH, Zhang JF. Advances and perspectives in carrier-free nanodrugs for cancer chemo-monotherapy and combination therapy. *Biomaterials* 2021;**268**:120557.
8. Chen XJ, Zou JF, Zhang K, Zhu JJ, Zhang Y, Zhu ZH, et al. Photothermal/matrix metalloproteinase-2 dual-responsive gelatin nanoparticles for breast cancer treatment. *Acta Pharm Sin B* 2021;**11**:271−82.
9. Ren JJ, Zhang L, Zhang JY, Zhang W, Cao Y, Xu ZG, et al. Light-activated oxygen self-supplied starving therapy in near-infrared (NIR) window and adjuvant hyperthermia-induced tumor ablation with an augmented sensitivity. *Biomaterials* 2020;**234**:119771.
10. Cheng Y, Bao DD, Chen XJ, Wu YJ, Wei YH, Wu ZB, et al. Microwave-triggered/HSP-targeted gold nano-system for triple-negative breast cancer photothermal therapy. *Int J Pharm* 2021;**593**:120162.
11. Piao JG, Gao F, Li YN, Yu L, Liu D, Tan ZB, et al. pH-sensitive zwitterionic coating of gold nanocages improves tumor targeting and photothermal treatment efficacy. *Nano Res* 2018;**11**:3193−204.
12. Day NB, Wixson WC, Shields CW. Magnetic systems for cancer immunotherapy. *Acta Pharm Sin B* 2021;**11**:2172−96.
13. Shen ZJ, Xia JF, Ma QM, Zhu W, Gao Z, Han SC, et al. Tumor microenvironment-triggered nanosystems as dual-relief tumor hypoxia immunomodulators for enhanced phototherapy. *Theranostics* 2020;**10**:9132−52.
14. Zeng K, Xu QF, Ouyang J, Han YJ, Sheng JP, Wen M, et al. Coordination nanosheets of phthalocyanine as multifunctional platform for imaging-guided synergistic therapy of cancer. *ACS Appl Mater Interfaces* 2019;**11**:6840−9.
15. Zhao ZH, Xu K, Fu C, Liu H, Lei M, Bao JF, et al. Interfacial engineered gadolinium oxide nanoparticles for magnetic resonance imaging guided microenvironment-mediated synergetic chemodynamic/photothermal therapy. *Biomaterials* 2019;**219**:119379.
16. Wang J, Dong Y, Li YW, Li W, Cheng K, Qian Y, et al. Designer exosomes for active targeted chemo-photothermal synergistic tumor therapy. *Adv Funct Mater* 2018;**28**:1707360.
17. Yang Y, Liu JJ, Liang C, Feng LZ, Fu TT, Dong ZL, et al. Nanoscale metal-organic particles with rapid clearance for magnetic resonance imaging-guided photothermal therapy. *ACS Nano* 2016;**10**:2774−81.
18. Wang ZY, Chen Z. Acute promyelocytic leukemia: from highly fatal to highly curable. *Blood* 2008;**111**:2505−15.
19. Dilda PJ, Hogg PJ. Arsenical-based cancer drugs. *Cancer Treat Rev* 2007;**33**:542−64.
20. Lu YP, Han SP, Zheng HY, Ma R, Ping YT, Zou JF, et al. A novel RGDyC/PEG co-modified PAMAM dendrimer-loaded arsenic trioxide of glioma targeting delivery system. *Int J Nanomed* 2018;**13**:5937−52.
21. Shi XW, Ma R, Lu YP, Cheng Y, Fan XD, Zou JF, et al. iRGD and TGN co-modified PAMAM for multi-targeted delivery of ATO to gliomas. *Biochem Biophys Res Commun* 2020;**527**:117−23.
22. Tao JY, Fei WD, Tang HX, Li CQ, Mu CF, Zheng HY, et al. Angiopep-2-conjugated "core-shell" hybrid nanovehicles for targeted and pH-triggered delivery of arsenic trioxide into glioma. *Mol Pharm* 2019;**16**:786−97.
23. Zhang BB, Chen XJ, Fan XD, Zhu JJ, Wei YH, Zheng HS, et al. Lipid/PAA-coated mesoporous silica nanoparticles for dual-pH-responsive codelivery of arsenic trioxide/paclitaxel against breast cancer cells. *Acta Pharmacol Sin* 2021;**42**:832−42.
24. Fu X, Li YS, Zhao J, Yu LL, Luo RG, Liang QR, et al. Will arsenic trioxide benefit treatment of solid tumor by nano-encapsulation? *Mini Rev Med Chem* 2020;**20**:239−51.
25. Fei WD, Zhang Y, Han SP, Tao JY, Zheng HY, Wei YH, et al. RGD conjugated liposome-hollow silica hybrid nanovehicles for targeted and controlled delivery of arsenic trioxide against hepatic carcinoma. *Int J Pharm* 2017;**519**:250−62.
26. Zhang Q, Vakili MR, Li XF, Lavasanifar A, Le XC. Polymeric micelles for GSH-triggered delivery of arsenic species to cancer cells. *Biomaterials* 2014;**35**:7088−100.
27. Luo XJ, Gong XQ, Su LY, Lin HY, Yang ZX, Yan XM, et al. Activatable mitochondria-targeting organoarsenic prodrugs for bioenergetic cancer therapy. *Angew Chem Int Ed Engl* 2021;**60**:1403−10.
28. Cioloboc D, Kurtz DM. Targeted cancer cell delivery of arsenate as a reductively activated prodrug. *J Biol Inorg Chem* 2020;**25**:441−9.
29. Huang RN, Lee TC. Cellular uptake of trivalent arsenite and pentavalent arsenate in KB cells cultured in phosphate-free medium. *Toxicol Appl Pharmacol* 1996;**136**:243−9.
30. Subbarayan PR, Ardalan B. In the war against solid tumors arsenic trioxide needs partners. *J Gastrointest Cancer* 2014;**45**:363−71.
31. Fu X, Liang QR, Luo RG, Li YS, Xiao XP, Yu LL, et al. An arsenic trioxide nanoparticle prodrug (ATONP) potentiates a therapeutic effect on an aggressive hepatocellular carcinoma model *via* enhancement of intratumoral arsenic accumulation and disturbance of the tumor microenvironment. *J Mater Chem B* 2019;**7**:3088−99.
32. Shi ZY, Chu CC, Zhang Y, Su ZJ, Lin HR, Pang X, et al. Self-assembled metal-organic nanoparticles for multimodal imaging-guided photothermal therapy of hepatocellular carcinoma. *J Biomed Nanotechnol* 2018;**14**:1934−43.
33. Liu CH, Wang DD, Zhang SY, Cheng YR, Yang F, Xing Y, et al. Biodegradable biomimic copper/manganese silicate nanospheres for chemodynamic/photodynamic synergistic therapy with simultaneous glutathione depletion and hypoxia relief. *ACS Nano* 2019;**13**:4267−77.
34. Wang WQ, Jin YL, Xu ZA, Liu X, Bajwa SZ, Khan WS, et al. Stimuli-activatable nanomedicines for chemodynamic therapy of cancer. *Wiley Interdiscip Rev Nanomed Nanobiotechnol* 2020;**12**:e1614.
35. Liu MD, Guo DK, Zeng RY, Ye JJ, Wang SB, Li CX, et al. Yolk-shell structured nanoflowers induced intracellular oxidative/thermal stress damage for cancer treatment. *Adv Funct Mater* 2020;**30**:2006098.
36. Fu LH, Hu YR, Qi C, He T, Jiang SS, Jiang C, et al. Biodegradable manganese-doped calcium phosphate nanotheranostics for traceable cascade reaction-enhanced anti-tumor therapy. *ACS Nano* 2019;**13**:13985−94.
37. Ding BB, Zheng P, Jiang F, Zhao YJ, Wang MF, Chang MY, et al. MnO(x) nanospikes as nanoadjuvants and immunogenic cell death drugs with enhanced antitumor immunity and antimetastatic effect. *Angew Chem Int Ed Engl* 2020;**59**:16381−4.
38. Tang HX, Li CQ, Zhang Y, Zheng HS, Cheng Y, Zhu JJ, et al. Targeted manganese doped silica nano GSH-cleaner for treatment of liver cancer by destroying the intracellular redox homeostasis. *Theranostics* 2020;**10**:9865−87.
39. Liu RF, Jing LJ, Peng D, Li Y, Tian J, Dai ZF. Manganese (II) chelate functionalized copper sulfide nanoparticles for efficient magnetic resonance/photoacoustic dual-modal imaging guided photothermal therapy. *Theranostics* 2015;**5**:1144−53.
40. Zhang L, Zhang ZW, Mason RP, Sarkaria JN, Zhao DW. Convertible MRI contrast: sensing the delivery and release of anti-glioma nanodrugs. *Sci Rep* 2015;**5**:9874.
41. Zhang K, Lin HY, Mao JJ, Luo XJ, Wei RX, Su ZZ, et al. An extracellular pH-driven targeted multifunctional manganese arsenite delivery system for tumor imaging and therapy. *Biomater Sci* 2019;**7**:2480−90.

42. Zhao ZH, Wang XM, Zhang ZJ, Zhang H, Liu HY, Zhu XL, et al. Real-Time monitoring of arsenic trioxide release and delivery by activatable T-1 imaging. *ACS Nano* 2015;**9**:2749−59.
43. Yang Y, Zhu WJ, Dong ZL, Chao Y, Xu L, Chen MW, et al. 1D coordination polymer nanofibers for low-temperature photothermal therapy. *Adv Mater* 2017;**29**:1703588.
44. Trachootham D, Alexandre J, Huang P. Targeting cancer cells by ROS-mediated mechanisms: a radical therapeutic approach? *Nat Rev Drug Discov* 2009;**8**:579−91.
45. Gorrini C, Harris IS, Mak TW. Modulation of oxidative stress as an anticancer strategy. *Nat Rev Drug Discov* 2013;**12**:931−47.
46. Yang Y, Wu H, Liu B, Liu Z. Tumor microenvironment-responsive dynamic inorganic nanoassemblies for cancer imaging and treatment. *Adv Drug Deliv Rev* 2021;**179**:114004.
47. Li CQ, Zhang K, Liu AD, Yue TX, Wei YH, Zheng HS, et al. MMP2-responsive dual-targeting drug delivery system for valence-controlled arsenic trioxide prodrug delivery against hepatic carcinoma. *Int J Pharm* 2021;**609**:121209.
48. Wang XW, Zhong XY, Liu Z, Cheng L. Recent progress of chemodynamic therapy-induced combination cancer therapy. *Nano Today* 2020;**35**:100946.
49. Chen PM, Pan WY, Luo PK, Phung HN, Liu YM, Chiang MC, et al. Pollen-mimetic metal-organic frameworks with tunable spike-like nanostructures that promote cell interactions to improve antigen-specific humoral immunity. *ACS Nano* 2021;**15**:7596−607.
50. Chu CC, Ren E, Zhang YM, Yu JW, Lin HR, Pang X, et al. Zinc(II)-dipicolylamine coordination nanotheranostics: toward synergistic nanomedicine by combined photo/gene therapy. *Angew Chem Int Ed Engl* 2019;**58**:269−72.
51. Tang Y, Lei TJ, Manchanda R, Nagesetti A, Fernandez-Fernandez A, Srinivasan S, et al. Simultaneous delivery of chemotherapeutic and thermal-optical agents to cancer cells by a polymeric (PLGA) nanocarrier: an *in vitro* study. *Pharm Res (N Y)* 2010;**27**:2242−53.
52. Zheng MB, Yue CX, Ma YF, Gong P, Zhao PF, Zheng CF, et al. Single-step assembly of DOX/ICG loaded lipid-polymer nanoparticles for highly effective chemo-photothermal combination therapy. *ACS Nano* 2013;**7**:2056−67.
53. Yang JL, Dai J, Wang Q, Cheng Y, Guo JJ, Zhao ZJ, et al. Tumor-triggered disassembly of a multiple-agent-therapy probe for efficient cellular internalization. *Angew Chem Int Ed Engl* 2020;**59**:20405−10.
54. Guo P, Liu DX, Subramanyam K, Wang BR, Yang J, Huang J, et al. Nanoparticle elasticity directs tumor uptake. *Nat Commun* 2018;**9**:130.
55. Ma C, Wu MJ, Ye WF, Huang ZW, Ma XY, Wang WH, et al. Inhalable solid lipid nanoparticles for intracellular tuberculosis infection therapy: macrophage-targeting and pH-sensitive properties. *Drug Deliv Transl Res* 2021;**11**:1218−35.
56. Meng XY, Chen LZ, Lv RM, Liu M, He NY, Wang ZF. A metal-phenolic network-based multifunctional nanocomposite with pH-responsive ROS generation and drug release for synergistic chemodynamic/photothermal/chemo-therapy. *J Mater Chem B* 2020;**8**:2177−88.
57. Egloff-Juras C, Bezdetnaya L, Dolivet G, Lassalle HP. NIR fluorescence-guided tumor surgery: new strategies for the use of indocyanine green. *Int J Nanomed* 2019;**14**:7823−38.
58. Li SK, Zhang WJ, Xing RR, Yuan CQ, Xue HD, Yan XH. Supramolecular nanofibrils formed by coassembly of clinically approved drugs for tumor photothermal immunotherapy. *Adv Mater* 2021;**33**:2100595.